

Article

An Activatable Nanoscintillator Probe for Detecting Telomerase Activity and Screening Inhibitors In Vivo

Baoliu Chen ¹, Junduan Dai ¹, Sijie Song ¹, Xianzhe Tang ¹, Yuheng Guo ¹, Ting Wu ¹, Mengnan Wu ¹, Chaojie Hao ¹, Xiaofeng Cheng ¹, Xucong Lin ², Yijie Bian ³, Zhaowei Chen ^{1,*}  and Huanghao Yang ^{1,*}

¹ MOE Key Laboratory for Analytical Science of Food Safety and Biology, New Cornerstone Science Laboratory, Fujian Provincial Key Laboratory of Analysis and Detection Technology for Food Safety, and State Key Laboratory of Photocatalysis on Energy and Environment, College of Chemistry, Fuzhou University, Fuzhou 350108, China

² Engineering Technology Research Center on Reagent and Instrument for Rapid Detection of Product Quality and Food Safety in Fujian Province, College of Chemistry, Fuzhou University, Fuzhou 350108, China

³ College of Biological Science and Engineering, Fuzhou University, Fuzhou 350108, China; bianyijie@fzu.edu.cn

* Correspondence: chenzw@fzu.edu.cn (Z.C.); hhyang@fzu.edu.cn (H.Y.)

Abstract: Telomerase represents an essential molecular machinery for tumor occurrence and progression and a potential therapeutic target for cancer treatment. Sensitive and reliable analysis of telomerase activity is of significant importance for the diagnosis and treatment of cancer. In this study, we developed a telomerase-activated nanoscintillator probe for deep-tissue and background-free imaging of telomerase activity and screening telomerase inhibitors in tumor-bearing living mice models. The probe was constructed by modifying lanthanide-doped nanoscintillators with aptamer-containing DNA anchor strands which hybridized with quencher labelled-oligonucleotide strands and telomerase primers. The X-ray-induced fluorescence of the probe was quenched originally but turned on upon telomerase-catalyzed extension of the primer. Benefiting from exceptional tissue penetrating properties and negligible autofluorescence of X-ray excitation, this probe enabled direct detection of telomerase activity in vivo via fluorescence imaging. Furthermore, with the direct, readable fluorescent signals, the probe enabled the screening of telomerase inhibitors in living cells and whole-animal models in the native states of telomerase. This strategy would inspire the development of low autofluorescence and deep tissue bioimaging probes for disease diagnosis and drug development in high-level living settings.

Keywords: bioimaging; nanoscintillator; telomerase; drug screening; cancer



Citation: Chen, B.; Dai, J.; Song, S.; Tang, X.; Guo, Y.; Wu, T.; Wu, M.; Hao, C.; Cheng, X.; Lin, X.; et al. An Activatable Nanoscintillator Probe for Detecting Telomerase Activity and Screening Inhibitors In Vivo. *Targets* **2023**, *1*, 34–47. <https://doi.org/10.3390/targets1010004>

Academic Editor: Rafik Naccache

Received: 22 May 2023

Revised: 9 June 2023

Accepted: 12 June 2023

Published: 14 June 2023



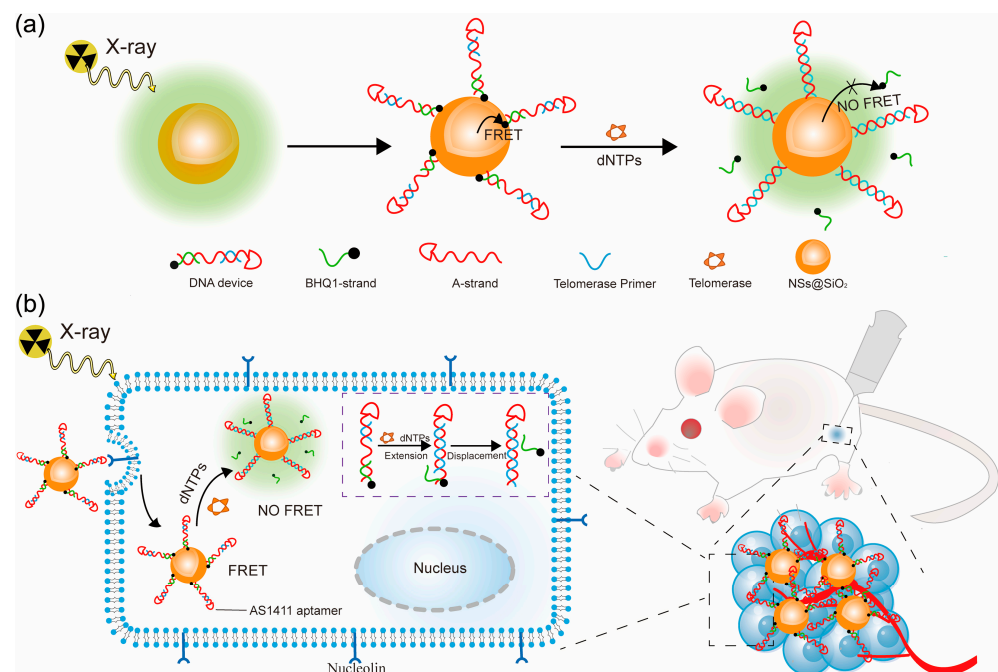
Copyright: © 2023 by the authors. Licensee MDPI, Basel, Switzerland. This article is an open access article distributed under the terms and conditions of the Creative Commons Attribution (CC BY) license (<https://creativecommons.org/licenses/by/4.0/>).

1. Introduction

Telomerase is a ribonucleoprotein reverse transcriptase that synthesizes telomeric DNA repeats at chromosome termini with an internal RNA template to compensate for the ‘end-replication problem’ [1,2]. Usually, telomerase activity is strictly repressed in most normal cells but greatly activated in a majority of tumor cells (85–90%) because the maintenance of telomere length by overexpressed telomerase is essential for tumors to escape the replicative senescence and crisis [3]. In this sense, telomerase has received enormous attention as an appealing molecular marker for cancer diagnosis and anticancer drug discovery [4–6]. This has spurred the development of polymerase chain reaction-based telomerase repeat amplification protocol (PCR-TRAP), the most classic method for analyzing telomerase activity in cell and tissue lysates [7,8]. To minimize the artifacts caused by PCR, modified TRAP methods have been developed by combining with electrochemical [9,10] and optical technologies [11]. However, these methods still face interferences from cell lysates, not to mention the requirement of time-consuming procedures for sample preparation. Alternatively, given the high sensitivity, straightforwardness, and non-invasiveness of fluorescence

imaging, various fluorescent probes have been attempted to directly visualize telomerase activity in living cells [12–14] and even in vivo [15,16]. Nevertheless, these probes are not without shortcomings, including the photobleaching of fluorophores, autofluorescence from biological specimens, and limited tissue penetration depth of UV/visible (UV/vis) excitation light sources [17,18]. Along this line, the development of a more reliable fluorescent probe overcoming these issues would allow better interrogation of the information on telomerase in its native physiological state.

Towards this goal, here, we developed an activatable nanoscintillator probe for tracking telomerase activity and screening telomerase inhibitors in vivo. Nanoscintillators are a class of luminescent nanomaterials that can absorb and convert ionizing radiation (X-rays, γ -rays, etc.) into UV/vis/near-infrared photons [19]. Of note, the exceptional penetration depth of the excitation sources (i.e., X-rays), avoidance of autofluorescence, and optical stability have enabled broad applications of nanoscintillators in the biomedical field [20–22]. In this study, we leveraged core-shell NaLuF₄:Tb/Gd@NaYF₄ nanoscintillators (NSs) and telomerase-responsive DNA molecular devices (DMDs) to construct a telomerase probe. As shown in Scheme 1, in the telomerase-responsive DMDs (Table S1), a long single-strand DNA (A-strand, 66 base, red) is covalently immobilized on the nanoscintillator surface and has three functional domains: an AS1411 aptamer sequence at the 3'-terminal for targeting cancer cells, the middle sequence for carrying telomerase primer (TP, blue), and the telomeric repeat-complementary sequence at the 5'-end for binding BHQ1 (black hole quencher 1)-labeled strand (BHQ1-strand, green). Initially, the fluorescence of nanoscintillators is quenched due to the proximity of BHQ1 to their surface. Once encountering telomerase, the extension of the TP strand displaces the BHQ1-labeled strand, turning on the fluorescence of nanoscintillators for signal readout. With systemic studies, we demonstrated the application of this probe for detecting telomerase activity in solution, living cells, and tumors, and screening telomerase inhibitors in animal models.



Scheme 1. Schematic illustration of the design and working principle of the nanoscintillator probe for detecting telomerase in vivo. (a) The X-ray-induced fluorescence of the nanoscintillators (NSs) is quenched by BHQ1 in the beginning due to the fluorescence resonance energy transfer (FRET) effect; upon telomerase-catalyzed extension of the primer, strand-displacement leads to the detachment of the BHQ1-strand from the surface of NSs and the FRET effect is inhibited, whereby the fluorescence of NSs is recovered for signal readout. (b) Specific recognition and internalization of probe into tumor cells for in vivo monitoring telomerase activity.

2. Materials and Methods

Additional information on reagents and materials, characterizations, experimental details, DNA sequences, and cell culture was given in the Supporting Information.

Synthesis of NaLuF₄:Tb(15%)/Gd(25%) nanoparticles. In a typical experiment, a mixture of Ln(CH₃COO)₃·4H₂O (0.5 mmol; Ln = Lu, Gd, Tb at the desired ratio), 4 mL oleic acid (OA), and 16 mL 1-octadecene (ODE) were added to a 50 mL two-neck round-bottom flask. Then, the resultant mixture was heated to 160 °C under vacuum for 45 min. After cooling the solution to room temperature, 10 mL methanol containing 1.25 mmol NaOH and 2 mmol NH₄F were added to the reaction system and stirred for 30 min at 50 °C, followed by heating to 100 °C for another 10 min under vacuum. Thereafter, the solution was heated to 300 °C at a rate of 20 °C/min and kept at 300 °C for 60 min under a nitrogen atmosphere while stirring. After cooling to room temperature, the resultant nanoparticles were collected by precipitation with ethanol and centrifugation at 8000 rpm and washed with ethanol and cyclohexane (1:1, *v/v*) three times. Finally, the obtained nanoparticles were redispersed in 5 mL cyclohexane.

Synthesis of NaLuF₄:Tb(15%)/Gd(25%)@NaYF₄ (NSs). In a typical procedure, 0.5 mmol Y(CH₃COO)₃·4H₂O, 5 mL OA and 7.5 mL ODE were added to a two-neck round-bottom flask, and then the resultant mixture was heated to 160 °C under vacuum for 50 min. After cooling the solution to room temperature, the core NaLuF₄:Tb(15%)/Gd(25%) nanoparticles dispersed in 4 mL cyclohexane were added to the reaction system, and the suspension was heated at 80 °C for 20 min to evaporate the cyclohexane. After cooling to room temperature, 10 mL methanol containing 1.25 mmol NaOH and 2 mmol NH₄F were added to the reaction system and stirred at 50 °C for 30 min, and then the resultant mixture was heated to 80 °C for another 20 min under vacuum to evaporate the methanol. The suspension was then heated to 290 °C at a rate of 20 °C/min and kept at 290 °C for 90 min under a nitrogen atmosphere while stirring. After cooling to room temperature, the nanoparticles were collected by precipitation with ethanol and centrifugation at 8000 rpm and washed with ethanol and cyclohexane (1:1, *v/v*) three times. Finally, the nanoparticles were redispersed in 5 mL cyclohexane and stored at 4 °C for further use.

Synthesis of silica-coated NSs (NSs@SiO₂) particles. 1-hexanol (2 mL), Triton X-100 (2 mL), and cyclohexane (10 mL) were mixed and stirred until the mixture became clear. Then, 300 µL deionized water and NSs solution dispersed in cyclohexane (4 mL 0.01 M) were sequentially added to the solution. The resultant mixture was stirred for 10 min at room temperature before the addition of 80 µL tetraethyl orthosilicate. After further vigorously stirring the suspension for 20 min, ammonium hydroxide (160 µL) was added, and the mixture was stirred at room temperature for 20 h. In the end, NSs@SiO₂ particles were collected by centrifugation at 8000 rpm and washed with ethanol three times.

Preparation of carboxyl group-functionalized NSs@SiO₂ (NSs@SiO₂-COOH) particles. NSs@SiO₂ particles (180 mg) were first dispersed in isopropyl alcohol (120 mL), 3-aminopropyltriethoxysilane (200 µL) was then added to the suspension, and the resultant suspension was refluxed in an oil bath at 85 °C for 10 h. The resultant nanoparticles (NSs@SiO₂-NH₂) were collected by centrifugation at 10,000 rpm for 10 min and washed with deionized water and ethanol. Sequentially, to prepare NSs@SiO₂-COOH particles, NSs@SiO₂-NH₂ particles (120 mg) were dispersed in *N,N*-dimethylformamide, and succinic anhydride (190 mg) was added to the suspension, which was further stirred at room temperature for 20 h. Thereafter, the resulting nanoparticles were collected by centrifugation at 10,000 rpm and washed with deionized water three times.

Preparation of the probe. NSs@SiO₂-COOH (2 mg) particles were dispersed in 2-(*N*-morpholino) ethanesulfonic acid (MES) buffer (pH 6.0, 10 mM), then 60 µL *N*-(3-(dimethylamino) propyl)-*N*-ethylcarbodiimide (30 mg/mL) and 120 µL *N*-hydroxysuccinimide (50 mg/mL) were added to the suspension. After stirring for 30 min, the pH of the suspension was adjusted with PBS to neutral, and then amino functionalized A-strand (40 µL, 0.1 M) was added, followed by stirring at room temperature for 18 h. In the end, the resultant nanoparticles were collected by centrifugation at 10,000 rpm, washed with water (pH 7.4) for three times, and re-dispersed in

Tris-HCl buffer (10 mM Tris, pH 7.4, 250 mM NaCl, 100 mM KCl) for further use. Then, 1 mL of A-strand-grafted NSs@SiO₂ (1 mg/mL) dispersed in Tris-HCl buffer was incubated with 8 nmol of BHQ1-strand and 8 nmol of telomerase primer at room temperature for 12 h under shaking. The probe was collected by centrifugation at 10,000 rpm and washed with Tris-HCl buffer three times.

Telomerase Extraction. Telomerases were extracted from HeLa cells with CHAPS buffer. Firstly, HeLa cells (1.0×10^6) were collected and transferred in a centrifuge tube when HeLa cells were in the exponential growth stage. Secondly, HeLa cells were washed with iced PBS two times. Thirdly, the cells were transferred in the cold CHAPS lysis buffer (0.5% (*w/v*) CHAPS, 10 mM Tris, pH 7.5, 1 mM ethylene glycol-bis(β -aminoethylether)-*N,N,N',N'*-tetraacetic acid, 0.1 mM phenylmethanesulfonyl fluoride, 10% glycerol, and 1 mM MgCl₂) and incubated at 4 °C for 30 min. Then, the lysate was centrifuged (12,000 rpm) at 4 °C for 20 min. The supernatant was collected and stored at -80 °C for further use.

Detection of telomerase activity in vitro. To determine the telomerase-responsive character of the probe, the time-dependent fluorescence variation kinetics of the probe was performed. The probe (0.5 mg/mL) and deoxynucleotide solution mixture (dNTPs; 200 μ M) were added into TRAP buffer containing telomerase extracts from 100,000 HeLa cells, and then the mixture was incubated at 37 °C for different times (10, 20, 30, 40, 60, 100, and 120 min) and time-dependent variation in fluorescence intensity was recorded. For comparison, we used PBS to replace the telomerase extracts to record the changes in potential background fluorescence.

To investigate the relationship between X-ray-induced fluorescence signals and telomerase activity, dNTPs (200 μ M) and different amounts of telomerase extracts equivalent to different numbers (0, 100, 500, 1000, 2000, 5000, 10,000, 20,000, 50,000, 100,000) of HeLa, HepG2, or MCF-7 cells were added to TRAP buffer containing the probe (0.5 mg/mL) and then the resultant suspensions were incubated at 37 °C for 40 min before recording the X-ray-induced fluorescence of each group. The change in the fluorescence intensity at $\lambda = 546$ nm of the probe was plotted against the number of cells. The limit of detection (LOD) was calculated using the equation $LOD = 3\sigma/S$, where σ is the standard deviation of ten consecutive measurements of the blank, and S is the slope of the linear part of the plot.

To verify the specificity of the probe towards telomerase, a series of biomolecules (BSA, thrombin, GSH, trypsin, lysozyme, and glucose) were respectively added into TRAP buffers containing 0.5 mg/mL of the probe. Then, the resultant mixtures were incubated at 37 °C for 40 min, and the fluorescence was recorded at the end. To study the stability of the probe, the probe was incubated with PBS buffer, Dulbecco's modified Eagle's medium (DMEM), DMEM containing 10% fetal bovine serum (FBS), and saline (0.9% NaCl solution) at 37 °C, respectively, for a series of time (0, 1, 4, 8, 12, 24, 36, and 48 h). At these indicated time points, the X-ray-induced fluorescence and hydrodynamic size of the probe were recorded.

Detection of telomerase activity in living cells. To assess telomerase activity in living cells with the probe, 5×10^5 HeLa cells were first seeded in a 6-well plate. After 24 h incubation at 37 °C, the medium was removed, and the cells were washed with PBS, followed by the addition of fresh medium containing the probe (0.5 mg/mL), and the cells were incubated for different times (0, 1, 2, 3, 4, and 5 h). Thereafter, the cells were washed with PBS and digested by trypsin, and the cell suspensions of each group were collected for recording the X-ray-induced fluorescence intensity.

To detect the telomerase activity in different cancer cells, MCF-7, Caco-2, HepG2, and A549 cells were seeded in 6-well plates and cultured for 24 h; then, the culture medium was replaced with fresh medium containing the probe (0.5 mg/mL). After incubating for 6 h, cells were washed with PBS and digested by trypsin; the cell suspensions were collected for recording the X-ray-induced fluorescence intensity and imaging, respectively. Imaging was performed using the IVIS Lumina III Series system (PerkinElmer).

For intracellular telomerase inhibitor screening, HeLa cells (5×10^5) were seeded in a 6-well plate at 37 °C for 24 h, followed by replacing the culture medium with fresh culture medium containing different concentrations of epigallocatechin gallate (EGCG; 0, 5, 10, 15, 20, and 25 μ M), 3'-Azido-3'-deoxythymidine (AZT; 25 μ M), curcumin (25 μ M), Doxorubicin (Dox; 25 μ M), and 2-[(E)-3-naphthalen-2-ylbut-2-enoylamino]benzoic acid (BIBR1532; 25 μ M) for 6 h. Then, the cells were washed with PBS and fed with fresh culture medium containing the probe (0.5 mg/mL) for 4 h. Thereafter, the cells were digested by trypsin for recording the X-ray-induced fluorescence intensity and imaging, respectively.

Imaging of telomerase activity and screening telomerase inhibitors in vivo. All animal experiments were approved by the Institutional Animal Care and Use Committee of Fuzhou University (Protocol Number 013-20210218-006 and the date of approval is 18 February 2021). Nude mice (6–8 weeks, ~18–20 g) were purchased from Shanghai SLAC Laboratory Animal Co., Ltd. (Shanghai, China). To establish human cervix tumors in mice, 1×10^6 HeLa cells were dispersed in 50 μ L PBS buffer and then subcutaneously injected into the right hind leg of athymic nude mice. When the tumor volumes reached a size of 150–350 mm³, the probe or the mis-probe lacking telomerase primer dispersed in saline was injected intratumorally. Then, fluorescence imaging of tumors in the nude mice was performed at 0, 1, 2, 3, 4, and 5 h after administration of the probe (15 mg/kg, 50 μ L, in 0.9% saline) or control probe (15 mg/kg, 50 μ L, in 0.9% saline) using the IVIS Lumina III Series system (PerkinElmer, Waltham, MA, USA). Mice receiving intratumor injections of saline were set as the control. For screening telomerase inhibitors in vivo, 6 h after HeLa tumor-bearing mice treated with AZT (50 mg/kg), EGCG (50 mg/kg), curcumin (50 mg/kg), BIBIR1532 (50 mg/kg), or Dox (50 mg/kg) by intratumor injection, the mice were treated with the probe for 4 h, and then X-ray-induced fluorescence imaging was recorded.

Statistical analysis. The obtained data were expressed as the mean value \pm standard deviation (SD), and the statistical significance between groups was analyzed with one-way ANOVA and Tukey's post hoc tests using the software GraphPad Prism. Reported *p* values were classified as follows: **** *p* < 0.0001, *** *p* < 0.001, ** *p* < 0.01, and * *p* < 0.05. A value of *p* < 0.05 was considered statistically significant.

3. Results and Discussion

3.1. Synthesis and Characterization of the Probe

The detailed synthetic process of the probe is depicted in Figure S1. To construct the probe, lanthanide-doped core-shell nanoscintillators (NaLuF₄:Tb(15%)/Gd(25%)@NaYF₄) with sizes around 25 nm were first prepared according to our previous work [23] and then deposited with a c.a. 2 nm thick silica shell (NSs@SiO₂, Figure S2 and Figure 1a–c). The X-ray excited fluorescence spectra of NSs and NSs@SiO₂ particles showed that four characteristic emission bands at 489, 546, 584, and 612 nm, assigned to the ⁵D₄ → ⁷F_J (J = 6, 5, 4, 3) transitions of the Tb³⁺ luminescence center (Figure 1d). The deposition of silica shell showed no obvious impact on the emission characteristics of the NSs. Thereafter, the obtained NSs@SiO₂ particles were sequentially functionalized with amino and carboxyl groups (Figure S3), followed by grafting the A-strand. Finally, the TP and BHQ1-strand were hybridized into their complementary segments in the A-strand to form the telomerase-responsive DMDs. The conjugation of the DMDs was confirmed by the characteristic absorption bands of DNA at 260 nm and BHQ1 centered at 546 nm in the UV-vis absorption spectrum (Figure 1e) and a negatively charged zeta potential (Figure S4). The X-ray-induced fluorescent spectra of the probe showed that the emission of NSs was strongly quenched (Figure 1f) because the overlap of emission bands with the absorption spectrum of BHQ1 led to fluorescence resonance energy transfer (FRET). These results indicated the successful modification of DMDs to the surface of NSs@SiO₂. Finally, the content of the DNA device in the probe was measured to be about 0.499 nmol per mg probe by measuring the conjugated number of BHQ1-strands (Figure S5).

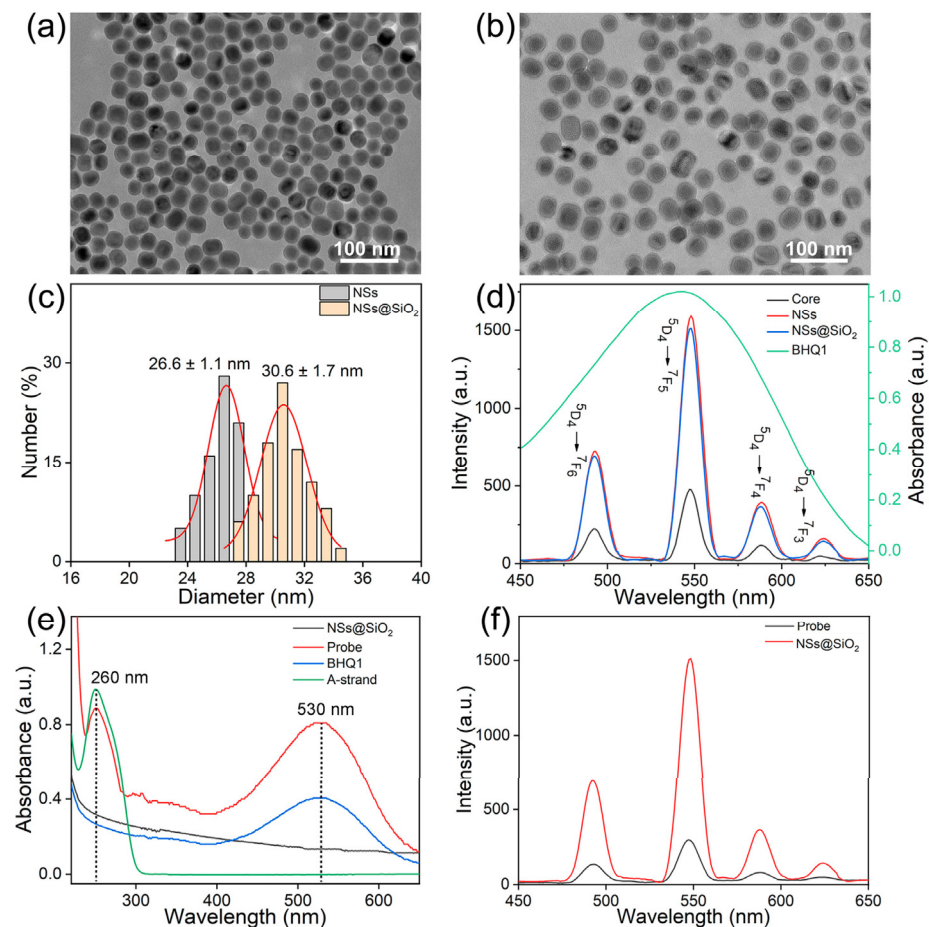


Figure 1. Synthesis and characterization of the probe. Representative TEM images of the as-prepared (a) NSs and (b) NSs@SiO₂ particles. (c) Size distributions of NSs and NSs@SiO₂ particles. (d) The normalized UV-vis absorption spectrum of BHQ1-strand (green line) and the X-ray-induced fluorescence spectra of the core nanoparticles (NaLuF₄:Tb(15%)/Gd(25%), black line), the core-shell NSs (red line), and NSs@SiO₂ particles (blue line). (e) UV-vis absorbance spectrum of NSs@SiO₂ particles, the probe, BHQ1, and A-strand DNA. (f) X-ray-induced fluorescence spectra of NSs@SiO₂ particles and the probe.

3.2. Telomerase Detection *In Vitro*

The strand-displacement behavior of DMDs by telomerase-triggered TP elongation was first validated by polyacrylamide gel electrophoresis (Figure S6). Then, the X-ray-induced fluorescence of the probe under different conditions was measured to confirm its feasibility for telomerase activity sensing. After incubating the probe with a mixture of deoxynucleotides (dNTPs) and telomerase extracts from 100,000 HeLa cells at 37 °C for 2 h, the X-ray-induced fluorescence intensity of the probe at 546 nm was significantly increased compared with that of the nontreated probe. In contrast, neither the extracts from the normal cell line (L02, normal human liver with limited expression of telomerase) nor the heat-inactivated HeLa cell extracts (95 °C for 20 min) induced obvious fluorescence enhancement. Moreover, minimal fluorescence enhancement was observed for a nonspecific probe lacking the TP strand (denoted as mis-probe) (Figure 2a). These results proved that telomerase could catalyze the extension of the TP strand and, thereafter, trigger the release of the BHQ1-strand via strand displacement. Concomitantly, the detachment of the BHQ1-strand from the surface of the NSs@SiO₂ reduced the FRET efficiency, recovering the fluorescence of NSs for signal readout.

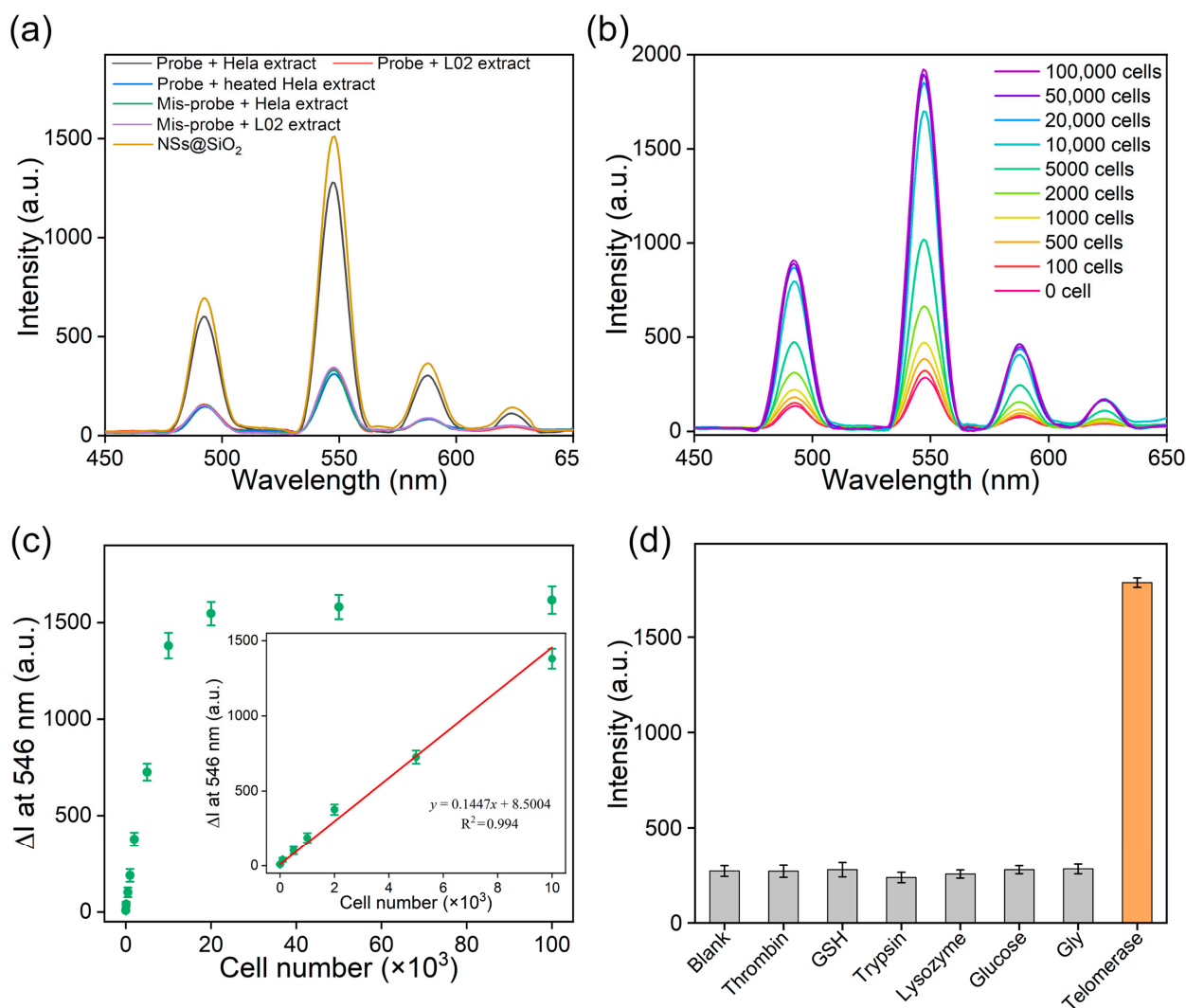


Figure 2. Sensitivity and selectivity of the probe. (a) X-ray-induced fluorescence spectra of suspensions containing the probe, dTNPs, and different analysts as indicated. Experiments conducted with the mis-probe were used as the control. The spectrum of an equal amount of NSs@SiO₂ particles was shown for better comparison. (b) X-ray-induced fluorescence spectra of the probe upon incubation with telomerase extracts from different numbers of HeLa cells. (c) The relationship between fluorescence intensity enhancement (ΔI) at 546 nm and HeLa cell numbers. Inset: linear plot of the ΔI versus HeLa cell numbers. (d) Fluorescence intensity at 546 nm of the probe after incubating with telomerase and different control analytes as indicated. Error bars represented the standard deviations of three independent experiments.

Next, we measured the time-dependent fluorescence variation kinetics of the probe by incubating it with dNTPs and telomerase extracted from 100,000 HeLa cells at 37 °C. As shown in Figure S7, the X-ray-induced fluorescence of the probe enhanced over time and reached a plateau within 40 min. Based on these results, 40 min of reaction time was chosen in the following experiments. Then, we tested the sensitivity of the probe by incubating it with telomerase extracts from different numbers of cells. As shown in Figure 2b, the intensity of X-ray-induced fluorescence increased gradually with increasing cell numbers, and there was a good linear relationship between the fluorescence enhancement (ΔI) at 546 nm and the telomerase activity equivalent to 0–10,000 HeLa cells (Figure 2c). Remarkably, the limit of detection was calculated to be 37 HeLa cells, which was comparable to the detection limit of most of the previously reported methods [24,25]. Furthermore, similar trends in the fluorescence changes were also observed for the probe after being treated

with telomerase extracts from different cancer cells, such as HepG2 (Figure S8) and MCF-7 cells (Figure S9), and the detection limits were measured to be 51 and 48 cells, respectively. These results suggested that this scintillating probe provided an alternative tool for the sensitive detection of telomerase activity.

We next evaluated the selectivity and stability of the probe. The selectivity of the probe was verified by incubating it with various biomolecules, including thrombin, glutathione (GSH), trypsin, lysozyme, glucose, and glycine. As shown in Figure 2d, the X-ray-induced fluorescence had no significant change upon incubating with the control analytes. In sharp contrast, a distinct fluorescence enhancement was observed in the presence of telomerase. These results demonstrated good sensing specificity of the developed probe for detecting telomerase even in complex biological media. Furthermore, we measured the stability of the probe by incubating the probe in PBS buffer, DMEM, DMEM plus 10% FBS, and saline for 48 h, which showed that the fluorescence intensity and hydrodynamic size of the probe changed negligibly (Figure S10). These results substantiated the stability of the probe in biorelevant aqueous environments.

3.3. Analysis of Intracellular Telomerase Activity

The probe was then employed for the monitoring of intracellular telomerase activity. To show whether the AS1411 aptamer in the probe could favor its uptake by cancer cells, we employed HeLa cells as the experimental cell line and L02 cells as a control. To directly visualize the cellular uptake of the probe under confocal laser scanning microscopy (CLSM), we replaced the BHQ1 with Cy3. As shown in Figure S11, after incubating with HeLa cells, green fluorescence could be observed in the cytoplasm after 1 h of incubation, and the fluorescence intensity enhanced gradually with increasing incubation time and plateaued around 3 h. In contrast, although the fluorescence signal of Cy3 could be detected in the normal cells (L02), the intensity was much lower than that in HeLa cells at each time point. These results indicated that the probe could be preferably internalized by HeLa cells because AS1411 aptamer in stand A could specifically recognize and bind to nucleolin that is overexpressed on the surface of cancer cells [26,27]. We next evaluated the cytotoxicity of the probe by incubating it with HeLa and L02 cells at various concentrations; the cellular viabilities of both cell lines were almost not affected up to 200 µg/mL (Figure S12). These results indicated that the probe had a satisfactorily low cytotoxicity.

Before utilizing the probe for directly detecting intracellular telomerase activity, we assessed the autofluorescence of cell suspensions under X-ray excitation. As shown in Figure 3a, compared to the strong background fluorescence generated under UV light (365 nm) excitation, the autofluorescence was reduced by more than 99% upon excitation by X-ray. These results confirmed that the scintillator-based probe was reliable for analyzing target biomolecules such as telomerase in complex biological environments. We next leveraged the probe for tracking telomerase activity in living cells. After treating HeLa cells with the probe at different times, cells were digested, and the fluorescence intensity of cell suspensions was measured. As shown in Figure 3b, the fluorescence intensity at 546 nm gradually increased over incubation time, and the fluorescence enhancement reached a plateau around 4 h. By contrast, no significant enhancement in X-ray-induced fluorescence was observed in L02 cells over the same time. In additional experiments using the mis-probe, no obvious changes in X-ray-induced fluorescence were recorded in either HeLa cells or L02 cells, indicating that the enhancement in fluorescence in HeLa cells was due to the specific response of the probe to telomerase. Moreover, similar changes in X-ray-induced fluorescence were also observed in other four kinds of cancer cells (including MCF-7, Caco-2, HepG2, and A549 cells) after being treated with the probe (Figure 3c), showcasing the generality of the probe for sensing telomerase activity in different cancer cell lines. Compared with assays sensing telomerase activity from cellular extracts, directly detecting telomerase activity in living cells with our probe would more reliably reflect the activity of telomerase and related biological processes in the native state [28].

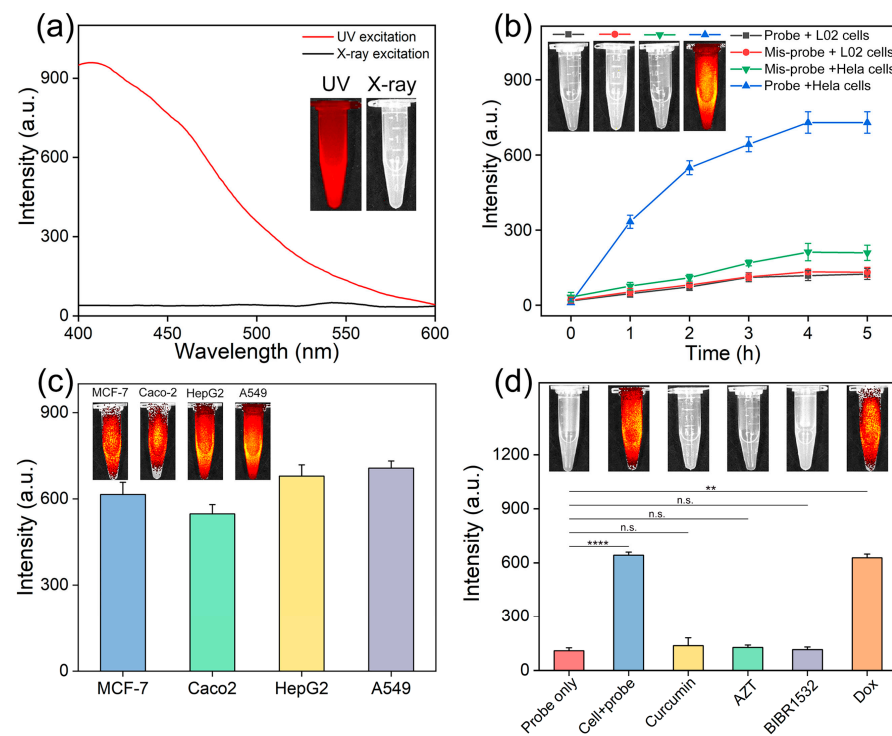


Figure 3. Sensing telomerase activity in living cells. (a) Fluorescence spectra of HeLa cell suspensions under UV and X-ray excitations; inset showed the corresponding photographs of the suspensions under different excitations. (b) Changes in the intensity of X-ray-induced fluorescence of the suspensions of HeLa cells and L02 cells after incubating with the probe and mis-probe for different times. Inset photographs showing the fluorescence images of the cell suspensions. (c) The fluorescence intensity and fluorescence images of suspensions of MCF-7, Caco-2, HepG2, and A549 cells after incubating with the probe for 4 h. (d) The fluorescence intensity and fluorescence images of HeLa cells after being treated with different drugs and the probe. The probe alone and nontreated HeLa cells plus probe (cell + probe) were set as controls. Error bars represented the standard deviations of three independent experiments. Statistical significance was calculated via ANOVA analysis with Tukey's post hoc test. ** $p < 0.01$, **** $p < 0.0001$. n.s., not significant.

3.4. Screening Telomerase Inhibitors in Living Cells

Telomerase inhibitors could be promising therapeutic drugs for cancer treatment, as most tumors rely on the reactivation of telomerase to maintain telomeres to preserve the proliferation potential while the telomerase activity of most normal cells is repressed [29,30]. Hence, it is of great significance to develop sensitive and selective tools for screening telomerase inhibitors. To confirm whether our probe could also be employed for evaluating the activity of inhibited telomerase and thus for screening telomerase inhibitors, EGCG was first studied as a representative inhibitor. As shown in Figure S13, 500,000 HeLa cells were treated with different concentrations of EGCG (0, 5, 10, 15, 20, and 25 μM) for 6 h before incubating with the probe. The fluorescence signals gradually declined upon increasing the doses of EGCG and reached a plateau above 20 μM , indicating that the probe could read out the dose-dependent inhibition of EGCG toward telomerase activity. Next, we employed the probe to screen telomerase inhibitors in living cells. Curcumin, AZT, and BIBR1532 were used as model drugs. These drugs inhibit telomerase activity by down-regulating human telomerase reverse transcriptase expression [31–34]. Dox was chosen as a control because its action is not directly associated with the telomerase activity. Afterward, these drugs were incubated with 500,000 HeLa cells for 6 h, and the cells were then treated with the probe. As shown in Figure 3d, negligible fluorescence enhancement was observed for groups treated with curcumin, AZT, and BIBR1532, which suggested that the telomerase activity was suppressed by these drugs. In contrast, the fluorescence signal in the Dox

group was similar to the control group treated with the probe only and much higher than that of the telomerase inhibitor-treated groups. These results demonstrated that the probe could be used for the monitoring of telomerase activity in drug-treated cancer cells and would be applicable for facilitating telomerase inhibitor screening in living cells.

3.5. In Vivo Imaging of Telomerase Activity

The use of visible or UV light as the excitation source for most in vivo imaging applications suffers from high tissue autofluorescence and low tissue penetration depth [17], which could affect the accuracy and reliability of signal outputs. The exceptional tissue penetrating and background-free characteristics of X-rays might solve these problems [19]. To this end, we first compared the autofluorescence background in Hela tumor-bearing mice under UV light and X-ray irradiations. As shown in Figure S14, there was almost no autofluorescence background in X-ray-excited imaging graphs, while an obvious fluorescence background signal was detected upon UV (365 nm) illumination. Next, the tissue penetration depth of X-ray-induced fluorescence imaging was studied by a tissue phantom study. Typically, capillary tubes were first filled with a telomerase-pretreated probe, and then pork of different thicknesses was placed between the capillary tubes and the X-ray source. As shown in Figure S15, X-ray-induced fluorescence imaging of the activated probe was clearly presented by X-ray excitation, even with a tissue thickness of 2.5 cm. These results indicated that the use of an X-ray-induced fluorescence imaging probe for detecting telomerase in vivo would essentially eliminate the autofluorescence background and achieve deep tissue imaging.

Encouraged by these results, we then employed the probe to directly visualize telomerase activity in Hela tumor-bearing athymic nude mice. The probe, mis-probe, or saline was injected into tumors, where mice treated with saline and the mis-probe were set as the control groups. The probe and mis-probe were dispersed in 0.9% saline solution (15 mg/kg, 50 μ L). As illustrated in Figure 4a, the fluorescence signal in the tumor of the probe group gradually increased over time and reached a maximum within 4 h post-injection under X-ray excitation. In contrast, the tumor fluorescence of the saline group and the mis-probe groups remained undetected and showed negligible variation over the same time. Consistently, quantitative analysis showed that the intratumoral fluorescence signal of the probe group revealed significantly much higher enhancement during 4 h post-injection, but no obvious intensity changed in the control groups (Figure 4b). These results indicated the feasibility of the probe for monitoring telomerase activity in vivo.

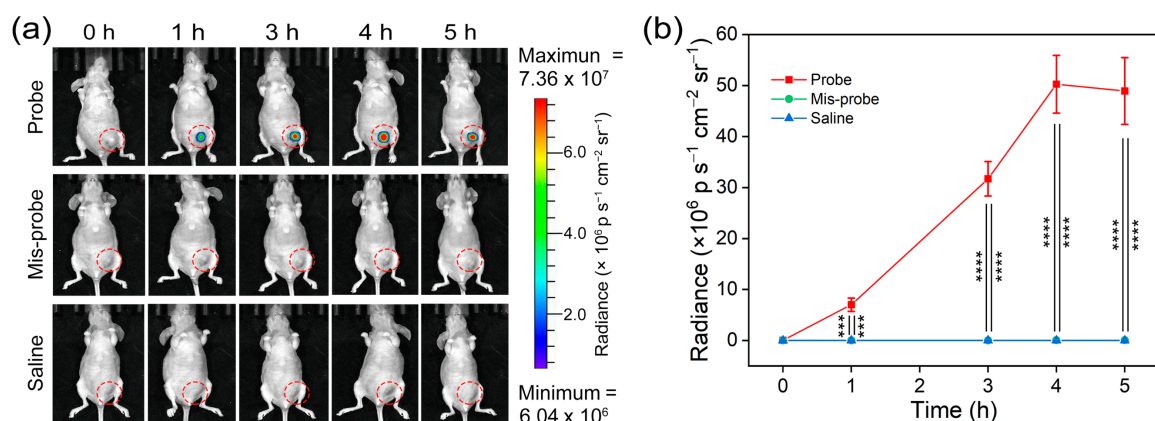


Figure 4. Imaging telomerase activity in vivo. (a) X-ray-induced fluorescence imaging of telomerase activity in Hela tumor-bearing athymic nude mice at different time points after intratumoral injection of the probe. Mice receiving intratumoral injection of saline and the mis-probe were utilized as the control groups. (b) Quantitative analysis of changes in the average fluorescence intensity in the tumor regions after receiving different treatments as shown in (a); p, photons; sr, steradian. Error bars represented the standard deviation of five mice. Statistical significance was calculated via ANOVA analysis with Tukey's post hoc test. *** $p < 0.001$, **** $p < 0.0001$.

To evaluate the biosafety of the probe in vivo, the body weight of mice was measured after administration of the probe. As shown in Figure S16, there was no significant change in the body weight of mice over 20 days post-injection. Additionally, standard hematoxylin-eosin (H&E) staining of the tissue sections of major organs (liver, spleen, heart, lungs, and kidneys) indicated that there were no obvious signs of pathological damage in comparison with the saline group (Figure S17). Moreover, the blood biochemistry tests showed that all blood parameters of hematological biomarkers (Figure S18) and organ function biomarkers (Figure S19) exhibited no statistical difference from the group treated with saline. These results validated the biosafety of the probe for bioimaging applications.

3.6. Telomerase Inhibitor Screening In Vivo

Although we have demonstrated that the probe could detect the activity of telomerase in inhibitor-treated living cells, two-dimensional cell culture condition cannot replicate the complexity of the three-dimensional tumor tissue architectures, and it is hard to reflect the interaction between the tumor microenvironment and cancer cells [35,36]. On the other hand, tumor-bearing animal models could closely recapitulate human pathology, providing a favorable preclinical tool for screening drugs before clinical testing [37]. Of note, the quality of information obtained has a strong correlation with the output measure [38].

Regarding that our probe could directly provide fluorescence readout of telomerase activity in tumor-bearing mice, we next studied the capacity of the probe for screening telomerase inhibitors in vivo. We chose curcumin (50 mg/kg body weight), AZT (50 mg/kg body weight), BIBR1532 (50 mg/kg body weight), EGCG (50 mg/kg body weight), and Dox (50 mg/kg body weight) as the model drugs. Hela-tumor-bearing mice of different groups were intratumorally injected with these drugs for 6 h before administration of the probe. Mice treated with PBS before administration of the probe were set as the blank control group. As shown in Figure 5a,b, the X-ray-induced fluorescence in the tumors of the groups treated with telomerase inhibitors (curcumin, EGCG, AZT, BIBR1532) was obviously lower than that of the blank control group. In comparison with the fluorescence variation in the control group, the X-ray-induced fluorescence changed negligibly in the group treated with Dox. These results indicated that in comparison with the conventional output method of screening drugs that evaluated the animal death or tumor volumes, our probe could provide an intuitional readout and allow more reliable and rapid measurement of the effects of telomerase-related drugs. This activatable nanoscintillator probe would provide a powerful tool for identifying telomerase-related anticancer drugs and could serve as a highly efficient platform for drug discovery. Moreover, it holds great potential to expand the concept of this design to develop novel tools for screening other target-related drugs.

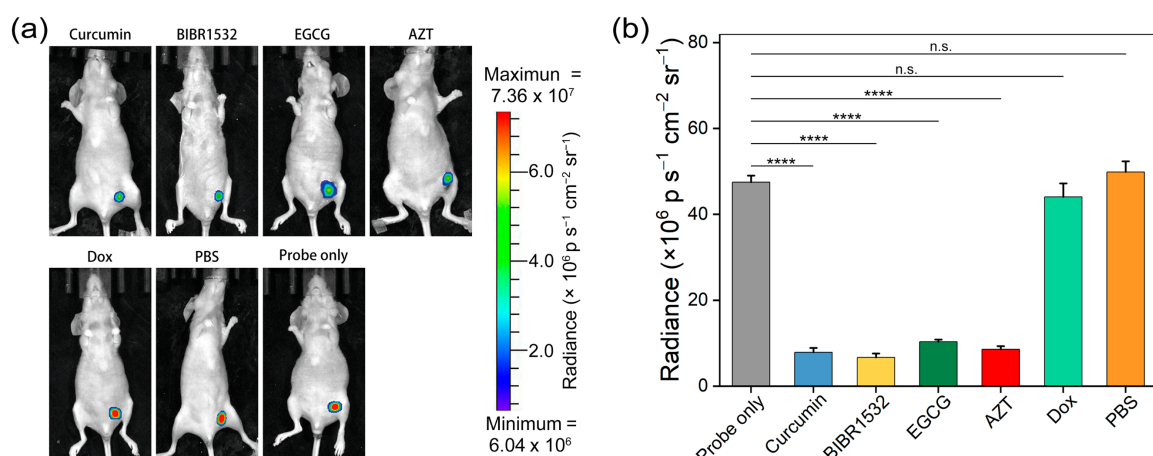


Figure 5. Telomerase inhibitor screening in vivo. (a) In vivo X-ray-induced fluorescence imaging of the HeLa tumor-bearing athymic nude mice after intratumoral injection of different drugs in PBS

(50 μ L, 50 mg/kg) and the probe (15 mg/kg, 50 μ L, in 0.9% saline solution). Mice receiving PBS (50 μ L) and the probe were used to exclude the possible effect of the drug vehicle. (b) Quantitative analysis of changes in the average fluorescence intensity in the tumor regions after receiving different treatments as shown in (a); p, photons; sr, steradian. Error bars represented the standard deviation of five mice. Statistical significance was calculated via ANOVA analysis with Tukey's post hoc test. **** $p < 0.0001$. n.s., not significant.

4. Conclusions

In summary, we have developed a novel probe by combining X-ray-excited nanoscintillators and telomerase-responsive DNA molecular devices for tracking telomerase activity and screening inhibitors in vivo. The proposed strategy outperformed the gold standard method of detecting telomerase activity measurement using PCR in terms of flexibility as it enabled telomerase activity sensing beyond cell lysates. The negligible autofluorescence background and high tissue penetration under X-ray excitation allowed the probe to directly visualize telomerase activity in living cells and tumor-bearing mice by producing turn-on fluorescence. More importantly, it is applicable to screen telomerase inhibitors in whole-animal models with easy-to-read fluorescent output signals. Overall, this study would inspire the development of advanced probes targeting different biomarkers for cancer diagnosis and anticancer drug discovery.

Supplementary Materials: The following supporting information can be downloaded at <https://www.mdpi.com/article/10.3390/targets1010004/s1>. Figure S1: Schematic illustration of the synthetic process of the probe. Figure S2: Synthesis and characterization of NaLuF₄:Tb/Gd nanoparticles. Figure S3: FTIR spectra of the oleate capped NaLuF₄:Tb/Gd@NaYF₄ (NSs), NSs@SiO₂, NSs@SiO₂-NH₂, and NSs@SiO₂-COOH particles. Figure S4: Zeta potential of NSs@SiO₂ particles (A), NSs@SiO₂-NH₂ particles (B), NSs@SiO₂-COOH particles (C), NSs@SiO₂-A-strand particles (D), and probe (E). Figure S5: Plot of the absorbance of BHQ1-strand at 546 nm versus the concentration of BHQ1-strand. Figure S6: Gel electrophoresis of the telomerase-responsive DNA devices (DMDs) and the telomerase-triggered telomerase primer extension and strand displacement. Figure S7: Fluorescence changes at 546 nm of the probe after incubation with telomerase extracts and PBS for different reaction times. Figure S8: (a) X-ray-induced fluorescence spectra of the probe after incubation with telomerase extracts from different numbers of HepG2 cells; (b) the relationship between fluorescence intensity enhancement (ΔI) at 546 nm and HepG2 cell numbers; inset: linear plot of the fluorescence enhancement versus HepG2 cell numbers. Figure S9: (a) X-ray-induced fluorescence spectra of the probe after incubation with telomerase extract from different numbers of MCF-7 cells; (b) the relationship between fluorescence intensity enhancement (ΔI) at 546 nm and MCF-7 numbers; inset: linear plot of the fluorescence enhancement versus MCF-7 cell numbers; Figure S10: The stability of the probe in different solutions after incubation at 37 °C for different times, and NSs@SiO₂ in these solutions was set as the control. Figure S11: Confocal laser scanning microscopy (CLSM) fluorescence images of (a) Hela cells and (b) L02 cells after treated with the probe for 0, 1, 2, 3, and 4 h. Figure S12: Cell viabilities of Hela and L02 cells after treated with different concentrations of the probe for 24 h. Figure S13: Inhibition of telomerase activity by EGCG. Figure S14: Comparison of the autofluorescence background under excitations of UV (365 nm) and X-ray source. Figure S15: Evaluation of the tissue penetration depth of X-ray. Figure S16: Body weight changes in healthy mice after intravenous injection of the probe and saline at different times. Figure S17: H&E-stained tissue sections of the major organs (heart, liver, spleen, lung, and kidney) after intravenous injection of the probe and 0.9% saline for 20 days. Figure S18: Hematology assays of healthy mice at days 10 and 20 after intravenous injection of the probe. Figure S19: Biochemical blood analysis of healthy mice at days 10 and 20 after intravenous injection of the probe; Table S1: DNA sequences in this work.

Author Contributions: Conceptualization, B.C., Y.B., Z.C. and H.Y.; methodology, B.C., J.D., S.S., X.T., Y.G., T.W., M.W., C.H., X.C., X.L., Y.B. and Z.C.; investigation, B.C., J.D., S.S., X.T., Y.G., T.W., M.W., C.H., X.C., X.L., Y.B. and Z.C.; resources, Y.B., Z.C. and H.Y.; writing—original draft preparation, B.C., Y.B., Z.C. and H.Y.; writing—review and editing, Y.B., Z.C. and H.Y.; supervision, Z.C. and H.Y.; project administration, Z.C. and H.Y.; funding acquisition, Z.C. and H.Y. All authors have read and agreed to the published version of the manuscript.

Funding: This work was funded by the National Key Research and Development Program of China (2020YFA0210800, H.Y.), the National Natural Science Foundation of China (22027805, H.Y.; 22107019, Z.C.; 22277011, Z.C.), and the Major Project of Science and Technology of Fujian Province (2020HZ06006, H.Y.). No APC was charged.

Institutional Review Board Statement: The animal study protocol was approved by the Institutional Animal Care and Use Committee of Fuzhou University (Protocol Number 013-20210218-006 and the date of approval is 18 February 2021).

Informed Consent Statement: Not applicable.

Data Availability Statement: All data generated or analyzed during this study are included in this published article (and its Supplementary Information files) or are available from the authors upon request.

Conflicts of Interest: The authors declare no conflict of interest.

References

1. Ghanim, G.E.; Fountain, A.J.; van Roon, A.-M.M.; Rangan, R.; Das, R.; Collins, K.; Nguyen, T.H.D. Structure of human telomerase holoenzyme with bound telomeric DNA. *Nature* **2021**, *593*, 449–453. [[CrossRef](#)] [[PubMed](#)]
2. Roake, C.M.; Artandi, S.E. Regulation of human telomerase in homeostasis and disease. *Nat. Rev. Mol. Cell Biol.* **2020**, *21*, 384–397. [[CrossRef](#)] [[PubMed](#)]
3. Soria, J.-C.; Gauthier, L.R.; Raymond, E.; Granotier, C.; Morat, L.; Armand, J.-P.; Boussin, F.o.D.; Sabatier, L. Molecular Detection of Telomerase-positive Circulating Epithelial Cells in Metastatic Breast Cancer Patients. *Clin. Cancer Res.* **1999**, *5*, 971–975.
4. Guterres, A.N.; Villanueva, J. Targeting telomerase for cancer therapy. *Oncogene* **2020**, *39*, 5811–5824. [[CrossRef](#)] [[PubMed](#)]
5. Harley, C.B. Telomerase and cancer therapeutics. *Nat. Rev. Cancer* **2008**, *8*, 167–179. [[CrossRef](#)]
6. Dai, J.; Liu, Z.; Wang, L.; Huang, G.; Song, S.; Chen, C.; Wu, T.; Xu, X.; Hao, C.; Bian, Y.; et al. A Telomerase-Activated Magnetic Resonance Imaging Probe for Consecutively Monitoring Tumor Growth Kinetics and In Situ Screening Inhibitors. *J. Am. Chem. Soc.* **2023**, *145*, 1108–1117. [[CrossRef](#)] [[PubMed](#)]
7. Krupp, G.; Kühne, K.; Tamm, S.; Klapper, W.; Heidorn, K.; Rott, A.; Parwaresch, R. Molecular basis of artifacts in the detection of telomerase activity and a modified primer for a more robust ‘TRAP’ assay. *Nucleic Acids Res.* **1997**, *25*, 919–921. [[CrossRef](#)] [[PubMed](#)]
8. Herbert, B.-S.; Hochreiter, A.E.; Wright, W.E.; Shay, J.W. Nonradioactive detection of telomerase activity using the telomeric repeat amplification protocol. *Nat. Protoc.* **2006**, *1*, 1583–1590. [[CrossRef](#)]
9. Wu, L.; Wang, J.; Ren, J.; Qu, X. Ultrasensitive Telomerase Activity Detection in Circulating Tumor Cells Based on DNA Metallization and Sharp Solid-State Electrochemical Techniques. *Adv. Funct. Mater.* **2014**, *24*, 2727–2733. [[CrossRef](#)]
10. Ling, P.; Lei, J.; Ju, H. Nanoscaled Porphyrinic Metal–Organic Frameworks for Electrochemical Detection of Telomerase Activity via Telomerase Triggered Conformation Switch. *Anal. Chem.* **2016**, *88*, 10680–10686. [[CrossRef](#)]
11. Zheng, G.; Daniel, W.L.; Mirkin, C.A. A New Approach to Amplified Telomerase Detection with Polyvalent Oligonucleotide Nanoparticle Conjugates. *J. Am. Chem. Soc.* **2008**, *130*, 9644–9645. [[CrossRef](#)] [[PubMed](#)]
12. Hong, M.; Xu, L.; Xue, Q.; Li, L.; Tang, B. Fluorescence Imaging of Intracellular Telomerase Activity Using Enzyme-Free Signal Amplification. *Anal. Chem.* **2016**, *88*, 12177–12182. [[CrossRef](#)]
13. Ma, W.; Fu, P.; Sun, M.; Xu, L.; Kuang, H.; Xu, C. Dual Quantification of MicroRNAs and Telomerase in Living Cells. *J. Am. Chem. Soc.* **2017**, *139*, 11752–11759. [[CrossRef](#)] [[PubMed](#)]
14. Wang, W.; Huang, S.; Li, J.; Rui, K.; Bi, S.; Zhang, J.-R.; Zhu, J.-J. Evaluation of intracellular telomerase activity through cascade DNA logic gates. *Chem. Sci.* **2017**, *8*, 174–180. [[CrossRef](#)] [[PubMed](#)]
15. Liu, Z.; Zhao, J.; Zhang, R.; Han, G.; Zhang, C.; Liu, B.; Zhang, Z.; Han, M.-Y.; Gao, X. Cross-Platform Cancer Cell Identification Using Telomerase-Specific Spherical Nucleic Acids. *ACS Nano* **2018**, *12*, 3629–3637. [[CrossRef](#)] [[PubMed](#)]
16. Ran, X.; Wang, Z.; Pu, F.; Ju, E.; Ren, J.; Qu, X. Nucleic acid-driven aggregation-induced emission of Au nanoclusters for visualizing telomerase activity in living cells and in vivo. *Mater. Horiz.* **2021**, *8*, 1769–1775. [[CrossRef](#)]
17. Frangioni, J.V. In vivo near-infrared fluorescence imaging. *Curr. Opin. Chem. Biol.* **2003**, *7*, 626–634. [[CrossRef](#)]
18. Liang, H.; Hong, Z.; Li, S.; Song, X.; Zhang, D.; Chen, Q.; Li, J.; Yang, H. An Activatable X-Ray Scintillating Luminescent Nanoprobe for Early Diagnosis and Progression Monitoring of Thrombosis in Live Rat. *Adv. Funct. Mater.* **2021**, *31*, 2006353. [[CrossRef](#)]
19. Chen, X.; Song, J.; Chen, X.; Yang, H. X-ray-activated nanosystems for theranostic applications. *Chem. Soc. Rev.* **2019**, *48*, 3073–3101. [[CrossRef](#)]
20. Pei, P.; Chen, Y.; Sun, C.; Fan, Y.; Yang, Y.; Liu, X.; Lu, L.; Zhao, M.; Zhang, H.; Zhao, D.; et al. X-ray-activated persistent luminescence nanomaterials for NIR-II imaging. *Nat. Nanotechnol.* **2021**, *16*, 1011–1018. [[CrossRef](#)] [[PubMed](#)]
21. Hong, Z.; Chen, Z.; Chen, Q.; Yang, H. Advancing X-ray Luminescence for Imaging, Biosensing, and Theragnostics. *Acc. Chem. Res.* **2023**, *56*, 37–51. [[CrossRef](#)]

22. Chen, Z.; Tsytsarev, V.; Finfrock, Y.Z.; Antipova, O.A.; Cai, Z.; Arakawa, H.; Lischka, F.W.; Hooks, B.M.; Wilton, R.; Wang, D.; et al. Wireless Optogenetic Modulation of Cortical Neurons Enabled by Radioluminescent Nanoparticles. *ACS Nano* **2021**, *15*, 5201–5208. [[CrossRef](#)]
23. Ou, X.; Qin, X.; Huang, B.; Zan, J.; Wu, Q.; Hong, Z.; Xie, L.; Bian, H.; Yi, Z.; Chen, X.; et al. High-resolution X-ray luminescence extension imaging. *Nature* **2021**, *590*, 410–415. [[CrossRef](#)]
24. Huang, J.; Zhu, L.; Ju, H.; Lei, J. Telomerase Triggered DNA Walker with a Superhairpin Structure for Human Telomerase Activity Sensing. *Anal. Chem.* **2019**, *91*, 6981–6985. [[CrossRef](#)] [[PubMed](#)]
25. Wang, J.; Wu, L.; Ren, J.; Qu, X. Visual detection of telomerase activity with a tunable dynamic range by using a gold nanoparticle probe-based hybridization protection strategy. *Nanoscale* **2014**, *6*, 1661–1666. [[CrossRef](#)] [[PubMed](#)]
26. Li, C.H.; Lv, W.Y.; Yan, Y.; Yang, F.F.; Zhen, S.J.; Huang, C.Z. Nucleolin-Targeted DNA Nanotube for Precise Cancer Therapy through Förster Resonance Energy Transfer-Indicated Telomerase Responsiveness. *Anal. Chem.* **2021**, *93*, 3526–3534. [[CrossRef](#)] [[PubMed](#)]
27. Lin, Y.; Huang, Y.; Yang, Y.; Jiang, L.; Xing, C.; Li, J.; Lu, C.; Yang, H. Functional Self-Assembled DNA Nanohydrogels for Specific Telomerase Activity Imaging and Telomerase-Activated Antitumor Gene Therapy. *Anal. Chem.* **2020**, *92*, 15179–15186. [[CrossRef](#)]
28. Verjans, E.-T.; Doijen, J.; Luyten, W.; Landuyt, B.; Schoofs, L. Three-dimensional cell culture models for anticancer drug screening: Worth the effort? *J. Cell. Physiol.* **2018**, *233*, 2993–3003. [[CrossRef](#)]
29. Ruparel, S.B.; Siddiq, A.; Marciniak, R.A. Targeting Telomerase for Cancer Therapy. *Curr. Cancer Ther. Rev.* **2011**, *7*, 215–226. [[CrossRef](#)]
30. Negrini, S.; De Palma, R.; Filaci, G. Anti-Cancer Immunotherapies Targeting Telomerase. *Cancers* **2020**, *12*, 2260. [[CrossRef](#)]
31. Rha, S.Y.; Izbicka, E.; Lawrence, R.; Davidson, K.; Sun, D.; Moyer, M.P.; Roodman, G.D.; Hurley, L.; Von Hoff, D. Effect of Telomere and Telomerase Interactive Agents on Human Tumor and Normal Cell Lines. *Clin. Cancer Res.* **2000**, *6*, 987–993. [[PubMed](#)]
32. Mittal, A.; Pate, M.S.; Wylie, R.C.; Tollefsbol, T.O.; Katiyar, S.K. EGCG down-regulates telomerase in human breast carcinoma MCF-7 cells, leading to suppression of cell viability and induction of apoptosis. *Int. J. Oncol.* **2004**, *24*, 703–710. [[CrossRef](#)] [[PubMed](#)]
33. Ramachandran, C.; Fonseca, H.B.; Jhabvala, P.; Escalon, E.A.; Melnick, S.J. Curcumin inhibits telomerase activity through human telomerase reverse transcriptase in MCF-7 breast cancer cell line. *Cancer Lett.* **2002**, *184*, 1–6. [[CrossRef](#)] [[PubMed](#)]
34. Pascolo, E.; Wenz, C.; Lingner, J.; Hael, N.; Priepke, H.; Kauffmann, I.; Garin-Chesa, P.; Rettig, W.J.; Damm, K.; Schnapp, A. Mechanism of Human Telomerase Inhibition by BIBR1532, a Synthetic, Non-nucleosidic Drug Candidate*. *J. Biol. Chem.* **2002**, *277*, 15566–15572. [[CrossRef](#)] [[PubMed](#)]
35. Barbosa, M.A.G.; Xavier, C.P.R.; Pereira, R.F.; Petrikaitė, V.; Vasconcelos, M.H. 3D Cell Culture Models as Recapitulators of the Tumor Microenvironment for the Screening of Anti-Cancer Drugs. *Cancers* **2022**, *14*, 190. [[CrossRef](#)]
36. Giacomotto, J.; Ségalat, L. High-throughput screening and small animal models, where are we? *Br. J. Pharmacol.* **2010**, *160*, 204–216. [[CrossRef](#)]
37. HogenEsch, H.; Nikitin, A.Y. Challenges in pre-clinical testing of anti-cancer drugs in cell culture and in animal models. *J. Control. Release* **2012**, *164*, 183–186. [[CrossRef](#)]
38. Debnath, A. Drug discovery for primary amebic meningoencephalitis: From screen to identification of leads. *Expert Rev. Anti. Infect. Ther.* **2021**, *19*, 1099–1106. [[CrossRef](#)]

Disclaimer/Publisher’s Note: The statements, opinions and data contained in all publications are solely those of the individual author(s) and contributor(s) and not of MDPI and/or the editor(s). MDPI and/or the editor(s) disclaim responsibility for any injury to people or property resulting from any ideas, methods, instructions or products referred to in the content.